JGR Space Physics

RESEARCH ARTICLE
10.1029/2023JA031488

Utilizing Helium Ion Chemistry to Derive Mixing Ratios of Heavier Neutral Species in Saturn's Equatorial Ionosphere

Joshua Dreyer[1,2], Erik Vigren[1], Fredrik L. Johansson[3], and J. Hunter Waite[4]

[1]Space Plasma Physics, Swedish Institute of Space Physics, Uppsala, Sweden, [2]Department of Physics and Astronomy, Uppsala University, Uppsala, Sweden, [3]European Space Research and Technology Centre, European Space Agency, Noordwijk, The Netherlands, [4]Waite Science LLC, Pensacola, FL, USA

Key Points:

- The dominant loss mechanism for He^+ ions in Saturn's equatorial ionosphere are reactions with heavier neutral species, not H_2
- The mixing ratio of volatiles in Saturn's ionosphere can be estimated from light ion and neutral measurements, using helium ion chemistry
- Comparing with other studies potentially suggests that only the most volatile species (CO, N_2 and CH_4) enter the atmosphere as vapor

Correspondence to:

J. Dreyer,
joshua.dreyer@rymdfysik.uu.se

Citation:

Dreyer, J., Vigren, E., Johansson, F. L., & Waite, J. H. (2023). Utilizing helium ion chemistry to derive mixing ratios of heavier neutral species in Saturn's equatorial ionosphere. *Journal of Geophysical Research: Space Physics*, *128*, e2023JA031488. https://doi.org/10.1029/2023JA031488

Received 14 MAR 2023
Accepted 3 JUN 2023

Abstract A surprisingly strong influx of organic-rich material into Saturn's upper atmosphere from its rings was observed during the proximal obits of the Grand Finale of the Cassini mission. Measurements by the Ion and Neutral Mass Spectrometer (INMS) gave insights into the composition of the material, but it remains to be resolved what fraction of the inferred heavy volatiles should be attributed as originating from the fragmentation of dust particles in the instrument versus natural ablation of grains in the atmosphere. In the present study, we utilize measured light ion and neutral densities to further constrain the abundances of heavy volatiles in Saturn's ionosphere through a steady-state model focusing on helium ion chemistry. We first show that the principal loss mechanism of He^+ in Saturn's equatorial ionosphere is through reactions with species other than H_2. Based on the assumption of photochemical equilibrium at altitudes below 2,500 km, we then proceed by estimating the mixing ratio of heavier volatiles down to the closest approaches for Cassini's proximal orbits 288 and 292. Our derived mixing ratios for the inbound part of both orbits fall below those reported from direct measurements by the INMS, with values of $\sim 2 \times 10^{-4}$ at closest approaches and order-of-magnitude variations in either direction over the orbits. This aligns with previous suggestions that a large fraction of the neutrals measured by the INMS stems from the fragmentation of infalling dust particles that do not significantly ablate in the considered part of Saturn's atmosphere and are thus unavailable for reactions.

Plain Language Summary During the final orbits of the Cassini mission, the spacecraft flew between Saturn's rings and the planets upper atmosphere. The onboard plasma instruments detected a large amount of ring particles falling toward the planet, but direct measurements of the composition of these grains are complicated due to the high spacecraft speed and instrumental effects. In this study, we present an independent method to estimate the abundance of heavier neutral species entering the atmosphere from infalling ring material. This method relies on helium ion chemistry and the measured light ion and neutral densities. Our results generally fall below those inferred from direct measurements. Together with comparisons to other studies, this potentially suggests that a large fraction of the infalling neutral species do not significantly ablate in the considered part of Saturn's atmosphere (and remain bound to the dust grains instead) and are thus unavailable for reactions.

1. Introduction

During its *Grand Finale*, the *Cassini* spacecraft dove into Saturn's upper atmosphere and sampled the composition in situ. Densities of volatiles heavier than H_2 and He were found to exceed predictions above the homopause, where the abundance of species such as CH_4 should decrease rapidly with increasing altitude due to their high mass (Yelle et al., 2018). This indicates an external source, and an influx of ring material at particularly high rates around the equator has been proposed (e.g., Perry et al., 2018; Waite et al., 2018).

The Ion and Neutral Mass Spectrometer (INMS) onboard Cassini operated in open source ion mode during a few of the passages through Saturn's upper atmosphere throughout the proximal orbits in 2017. Due to the high spacecraft velocity, exceeding 30 km/s, the retrieval of ion number densities from the INMS open source was limited to light ion species with masses (for singly charged species) of <8 Da (Cravens, Moore, et al., 2019; Waite et al., 2018). As a consequence, estimates of what species dominate the ion population near the ionospheric peak rely in part on indirect methods and modeling (e.g., Dreyer et al., 2021). Concerning neutrals, the difficulty in differentiating between products from impact fragmentation of infalling dust grains and ambient gas-phase species, as well as adsorption effects, complicated the analysis of the INMS data (Miller et al., 2020; Serigano

et al., 2022a; Waite et al., 2018). Consequently, number densities for heavier volatiles (e.g., H_2O, CH_4, NH_3, CO_2, N_2, and CO) are not necessarily well constrained. Recent modeling efforts are not able to reproduce some of the expected effects of the measured high influxes of these species on the ionospheric and stratospheric chemistry (Moses et al., 2023). The aim of the present study is to present an alternative indirect method to constrain mixing ratios of heavier volatiles in Saturn's ionosphere.

Previously H^+ and H_3^+ measurements have been used partly for similar purposes. Cravens, Moore, et al. (2019) empirically derived mixing ratios of M- and R-type molecules along Cassini's trajectory for orbit 288. They split molecules into M- and R-types based on reactivity with H^+ and H_3^+; M-type molecules react with both, R-type only with H_3^+. Vigren et al. (2022) conducted a similar study, adding grain charging to the modeling. They remarked that for altitudes near the closest approach of orbit 292 the derived mixing ratios of M-type and R-type species respectively succeeded and exceeded what had been reported from INMS measurements (Miller et al., 2020) by roughly an order of magnitude. This was referred to as a mixing ratio conundrum. The same issue was raised in a different way by Moore et al. (2018) who used INMS-measured neutral densities in their Saturn ionospheric model and reported severe difficulties in reproducing the observed H^+ and H_3^+ densities in the deep ionosphere. The conundrum remains unresolved, as further discussed by Moses et al. (2023), and the possibility of closing in on underlying causes was a central motivation behind the present study, which instead of focusing on H^+ and $H_3{}^+$, targets helium ions. That the concentration of He^+ is sensitive to the influx of heavier volatiles is mentioned briefly by Moses et al. (2023). Exploring this in a quantitative way was a further motivation of the present work.

Neutral helium is expected to be minimally affected by the aforementioned fragmentation and adsorption effects. Furthermore, ionized helium, He^+, reacts only slowly with molecular hydrogen. A consequence of this is that He^+ ions produced by, for example, photoionization of He in H_2-dominated ionospheres, such as those of Jupiter and Saturn, can have principal loss mechanisms other than through reactions with molecular hydrogen even if the other reactants are present in rather small volume mixing ratios. We will subsequently show that the main loss channels for He^+ in Saturn's upper atmosphere are charge-exchange reactions with heavier volatile species. We then use this to make an independent estimate of the mixing ratios of these volatiles through a simple model focusing on the production and loss balance of helium ions.

In the following Section 2 we describe the method in further detail. Our results are presented in Section 3 and the derived mixing ratios of heavy volatiles are compared to those derived from other indirect methods and those inferred from INMS observations. Concluding remarks are given in Section 4.

2. Method

The required number density measurements as described below are available for the proximal orbits 288 and 292 when limiting to orbits that reached altitudes <2,500 km.

As a starting hypothesis, we assume that He^+ is lost mainly through charge exchange reactions with heavier volatiles, since it reacts very slowly with H_2 and H (Barlow, 1984). We group the species acting as potential primary He^+ loss channels (H_2O, CH_4, NH_3, CO_2, N_2, and CO) as $\in$X. To test our starting hypothesis, we set out to compare the He^+ densities derived from a simple atmospheric photoionization model, assuming loss only via H_2, with those measured by the INMS. The INMS data is initially corrected for the time shift identified and described by Dreyer et al. (2022).

We start with the solar extreme ultraviolet (EUV) fluxes provided by the Laboratory for Atmospheric & Space Physics (LASP) Interactive Solar Irradiance Datacenter (LISIRD) as extrapolated to Saturn's orbit on the dates of Cassini's flybys 288 (2017-08-14) and 292 (2017-09-09), based on the Flare Irradiance Spectral Model (FISM-P, see Chamberlin et al., 2008). Using the INMS-measured H_2 densities and photoabsorption cross sections for H_2 compiled by Chadney et al. (2022), we calculate the attenuated EUV flux density for the relevant altitudes below 2,500 km using the Beer-Lambert law. A correction for the solar zenith angle is made under the approximation of a planar stratified atmosphere. Combining the attenuated EUV flux density spectrum at each consecutive altitude bin with the hydrogen and helium photoionization cross sections (Browning & Fryar, 1973; Cunto et al., 1993) from the PHIDRATES database (phidrates.space.swri.edu, Huebner & Mukherjee, 2015) yields the ionisation frequencies ν_{ion,H_2} and $\nu_{\mathrm{ion,He}}$ of H_2 and He, respectively. These ionisation frequency profiles enable us to set the

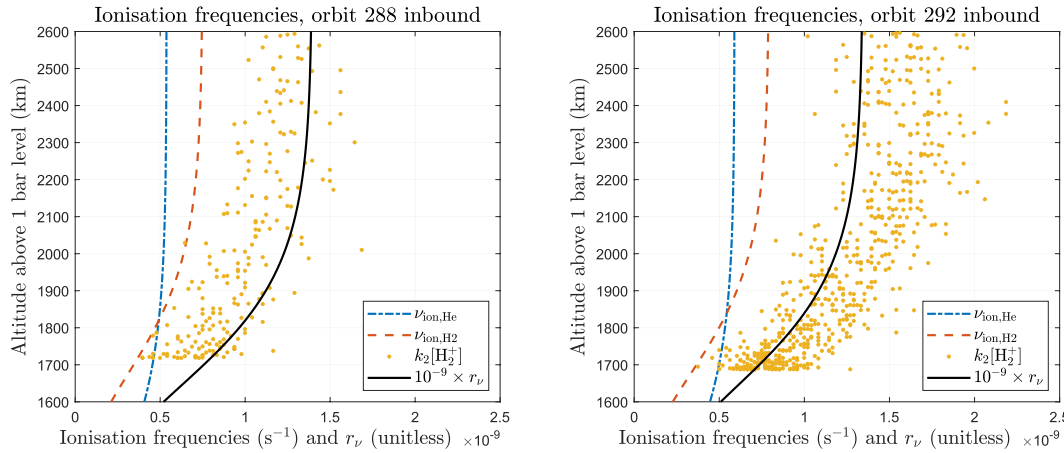

Figure 1. Comparison of modeled H_2 and He ionisation frequency profiles and the measurement-derived $\nu_{\mathrm{ion},H_2} = k_2[H_2^+]$ for the inbound parts of orbits 288 and 292. The ratio r_ν between the modeled profiles is scaled by a factor 10^{-9} and shown as the solid black line.

ratio $r_\nu = \nu_{\mathrm{ion},H_2}/\nu_{\mathrm{ion,He}}$ for each altitude bin. The calculated ionisation frequencies and r_ν for orbits 288 and 292 are shown in Figure 1.

In photochemical equilibrium (PCE), the production rate of H_2^+ equals its loss rate. The assumption of PCE is suitable at altitudes up to at least ~2,500 km in Saturn's equatorial ionosphere (Moore et al., 2018), assuming diffusion being the dominant transport process over ion drifts in this area and time scales for both exceeding those for chemical loss, and likely even higher for this species. The main production and loss channels for H_2^+ are

$$H_2 + h\nu \longrightarrow H_2^+ + e^- \quad (1)$$

$$H_2^+ + H_2 \longrightarrow H_3^+ + H, \quad (2)$$

where the second reaction has a rate coefficient $k_2 = 2.08 \times 10^{-9}$ cm^3 s^{-1} (Theard & Huntress, 1974). In PCE, $P(H_2^+) = L(H_2^+) = k_2[H_2^+][H_2] = \nu_{\mathrm{ion},H_2}[H_2]$. Our immediate goal is to utilize the INMS-measured H_2^+ densities as a proxy for the incoming solar EUV flux.

While we have a calculated EUV flux profile at hand it is to be noticed that the discrepancy between modeled and observed H_2^+ density profiles of up to 70% at high altitudes for orbit 292 (see Figure 1) is as pronounced as initially reported by Moore et al. (2018) and remains to be explained. We can circumvent the issue and assess the helium production rate via the measured H_2^+ densities and the presumably robust estimate of r_ν. To clarify, we utilize the measured H_2^+ number densities, the relation $k_2[H_2^+] = \nu_{\mathrm{ion},H_2}$ and divide by the above derived ratio r_ν to estimate the ionization frequency for helium. The production rate of He^+ can thus be expressed as

$$P(He^+) = \nu_{\mathrm{ion,He}}[He] = \frac{\nu_{\mathrm{ion},H_2}}{r_\nu}[He] = \frac{k_2}{r_\nu}[H_2^+][He]. \quad (3)$$

We proceed by estimating the He^+ density assuming loss only via the following reactions with H_2:

$$He^+ + H_2 \longrightarrow He + H^+ + H \quad (4)$$

$$He^+ + H_2 \longrightarrow He + H_2^+ \quad (5)$$

$$L(He^+) = k_3[He^+][H_2], \quad (6)$$

with $k_3 = (3.4 \times 10^{-14} + 7.2 \times 10^{-15})$ cm^3 s^{-1} (Barlow, 1984) being the sum of the rate coefficients for reactions 4 and 5 (assuming $T = 370$ K). The effects of choosing a lower or higher rate coefficient k_3 from the literature are discussed in Section 3. In photochemical equilibrium the production rate of He^+ equals its loss rate, $P(He^+) = L(He^+)$, and the He^+ number density can be estimated as:

$$[He^+] = \frac{k_2[H_2^+][He]}{k_3 r_\nu [H_2]} \quad (7)$$

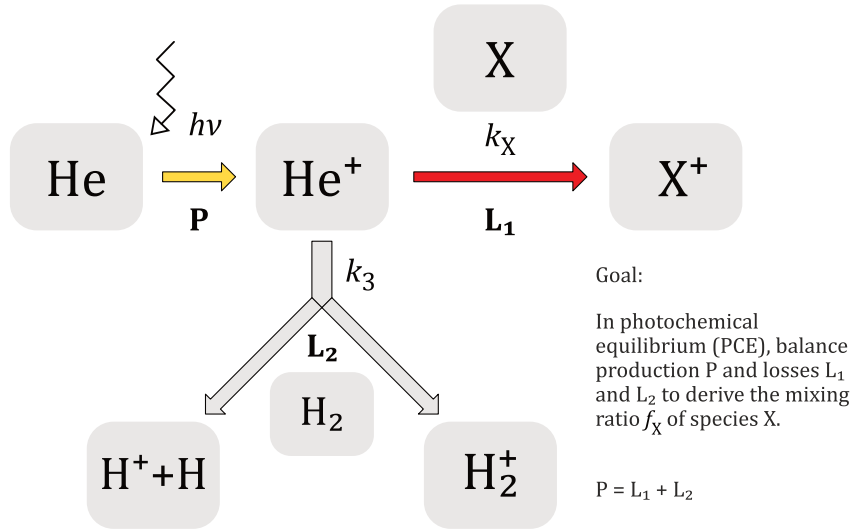

Figure 2. A schematic of the Helium ion chemistry that serves as the basis for the present study.

The assumption of PCE for H_2^+ is easily justified even to rather high altitudes due to the short lifetime of the ions on the order of ∼0.5 s, but this is not necessarily always true for helium ions due to their longer chemical lifetime. A simple check of the loss rate for He^+ ions via ion-neutral and charge-exchange reactions yields lifetimes of ∼200 s around closest approach, ∼1,500 s around 2,100 km and ∼9,000 s around 2,500 km. It is thus likely that ion-neutral diffusion can affect the assumption of PCE at the higher end of our analyzed altitude range, but the assumption should hold for most of it, when comparing to transport timescales based on Cravens, Morooka, et al. (2019). The helium ion chemistry is summarized in Figure 2 as a simple schematic.

Figure 3 shows that the estimated He^+ number densities exceed the measured densities by roughly an order of magnitude when assuming only loss via H_2. Interestingly, in the altitude range between ∼1,850–2,000 km for orbit 288 this discrepancy is sharply reduced to a factor 2 or less (indicated by the shaded area in Figure 3). This feature is discussed further in Section 3. Taken at face value it might indicate a locally and/or temporally lower abundance of species ∈X.

After this test, we proceed with our estimation for the mixing ratios of the volatile species ∈X, adding charge exchange reactions with these species to the main loss channels for He^+ ions:

$$\mathrm{L}\left(\mathrm{He}^+\right) = k_{\mathrm{X,He}^+}\left[\mathrm{He}^+\right][\mathrm{X}] + k_3\left[\mathrm{He}^+\right][\mathrm{H}_2]. \tag{8}$$

In PCE, $P(He^+) = L(He^+)$ and we can equate Equation 3 and Equation 8:

$$\frac{k_2}{r_v}\left[\mathrm{H}_2{}^+\right][\mathrm{He}] = k_{\mathrm{X,He}^+}\left[\mathrm{He}^+\right][\mathrm{X}] + k_3\left[\mathrm{He}^+\right][\mathrm{H}_2]. \tag{9}$$

With the mixing ratio of species ∈X expressed as $f_X = [X]/[H_2]$, we obtain

$$f_{\mathrm{X,He}^+} = \frac{k_2\left[\mathrm{H}_2{}^+\right][\mathrm{He}]}{r_v k_{\mathrm{X,He}^+}\left[\mathrm{He}^+\right][\mathrm{H}_2]} - \frac{k_3}{k_{\mathrm{X,He}^+}}. \tag{10}$$

For comparison, the equation to derive f_X from H_3^+ chemistry as given by Cravens, Moore, et al. (2019) is:

$$f_{\mathrm{X,H}_3^+} = \frac{k_2\left[\mathrm{H}_2{}^+\right]}{k_{\mathrm{X,H}_3^+}\left[\mathrm{H}_3{}^+\right]} - \frac{\alpha_{300,\mathrm{H}_3^+}\, n_e}{k_{\mathrm{X,H}_3^+}[\mathrm{H}_2]}, \tag{11}$$

where n_e is the electron number density and $\alpha_{300,\mathrm{H}_3^+} = 1.2 \times 10^{-7} \times (T_e/300\,\mathrm{K})^{-0.65}$ $\mathrm{cm}^3\ \mathrm{s}^{-1}$ (Sundström et al., 1994) is the thermal rate constant for the dissociative recombination of H_3^+, which depends on the electron temperature, T_e. We utilize the electron densities and temperatures as derived by Morooka et al. (2019) for this

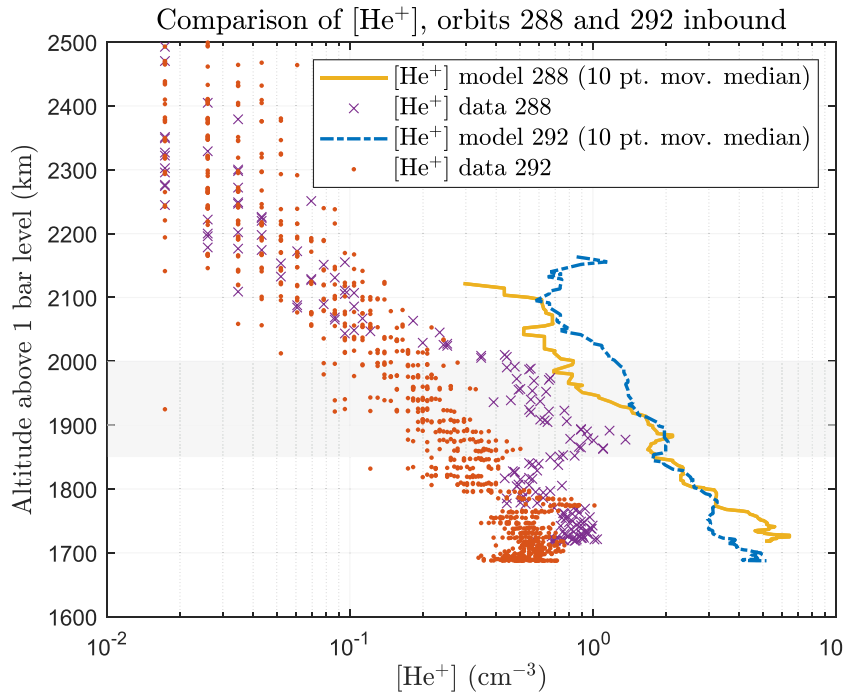

Figure 3. Comparison of measured He^+ number densities with model results (10 point moving median lines), assuming only loss via H_2 ion-neutral and charge-exchange reactions. The discrepancy between model and data abruptly decreases within the shaded area between 1850 and 2,000 km for orbit 288.

calculation, and it can be noted that overall the second term describing electron recombination is of much lesser importance than the first.

A survey of the UMIST database for astrochemistry (McElroy et al., 2013, udfa.ajmarkwick.net), from which all rate coefficients used in this study are obtained, reveals that the rate coefficients for the charge exchange reactions of He^+ ions with the species ∈X are 0.55–2.2 × 10^{-9} cm^3 s^{-1}, while the rate coefficients for the proton transfer reactions of H_3^+ ions with the species ∈X are 1.8–5.9 × 10^{-9} cm^3 s^{-1}, as outlined in Table 1. We adapt $k_{X,He^+} = 1.6 \times 10^{-9} cm^3\ s^{-1}$ and $k_{X,H_3^+} = 2.4 \times 10^{-9}\ cm^3\ s^{-1}$ as default values of the respective effective rate coefficient, while further exploring in Section 3 the effect of using the extremes of the values listed in Table 1. Particularly the rate coefficients for the reactions with H_2O are notable outliers among the values listed in Table 1.

3. Results and Discussion

Before discussing the results, it should be kept in mind that altitude and latitude are naturally not independent variables for Cassini's orbits and variations across a range of either could also be attributed to changes of the other

Table 1
Rate Coefficients Collected From the UMIST Database for Astrochemistry (McElroy et al., 2013, udfa.ajmarkwick.net) for Charge Exchange Reactions of He^+ Ions (Left of Slash) and for Proton Transfer Reactions of H_3^+ (Right of Slash) With Species ∈X

Reaction		Rate coefficient (10^{-9} cm^3 s^{-1})
$He^+/H_3^+ + H_2O$	⟶ He/H_2 + other species	0.55/5.9
$He^+/H_3^+ + CH_4$	⟶ He/H_2 + other species	1.81/2.4
$He^+/H_3^+ + NH_3$	⟶ He/H_2 + other species	2.2/4.39
$He^+/H_3^+ + CO_2$	⟶ He/H_2 + other species	1.14/2.0
$He^+/H_3^+ + N_2$	⟶ He/H_2 + other species	1.6/1.8
$He^+/H_3^+ + CO$	⟶ He/H_2 + other species	1.6/2.21

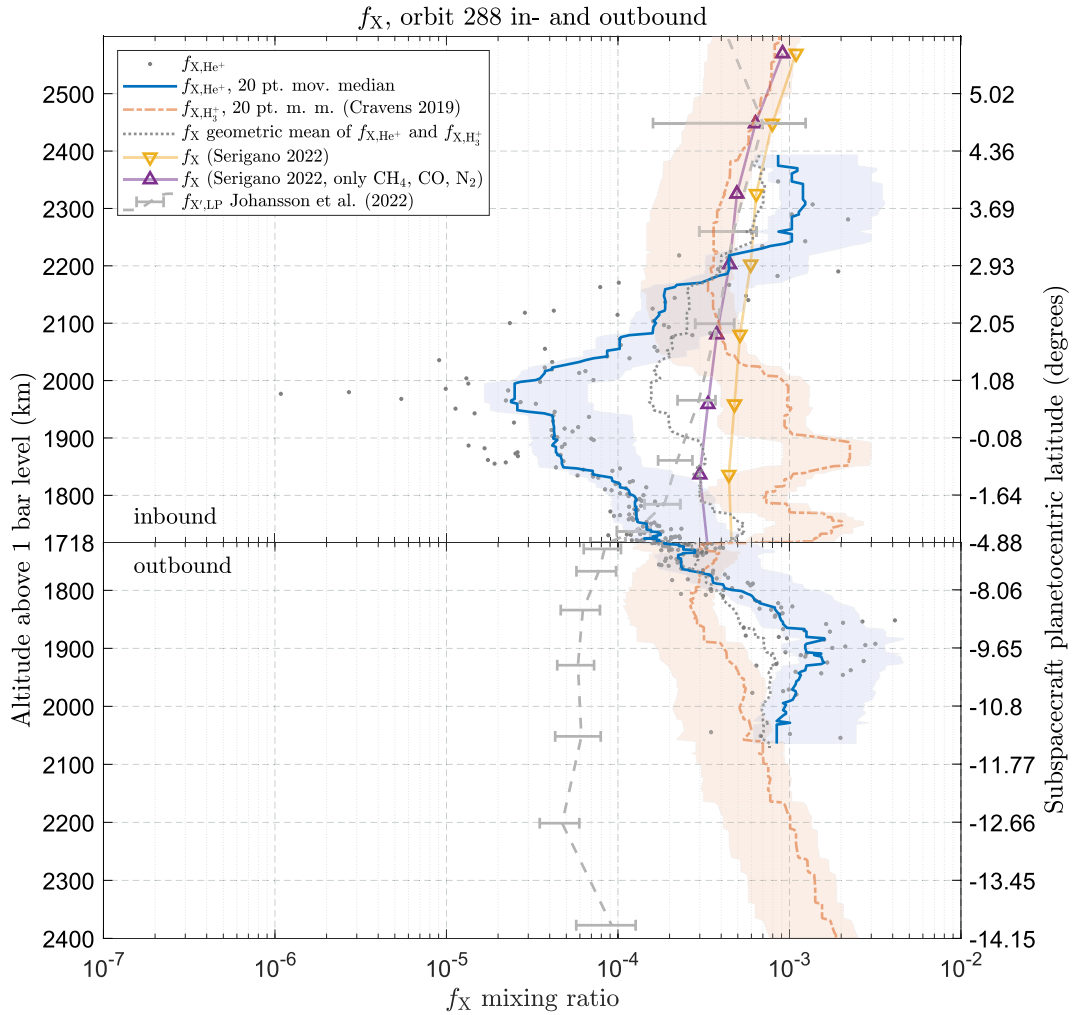

Figure 4. Mixing ratios f_X of species ∈X (in relation to H_2 density) for orbit 288 as gray dots, with a 20 point moving median as a blue line. The derived mixing ratio profile based on Equation 11 (Cravens, Moore, et al., 2019) is shown as a red dashed line (also 20 point moving mean), and a geometric mean of the two lines is shown as the dotted black line. The blue and red shaded areas around the lines mark the variation of f_X when setting k_X to the lowest or highest value, respectively (see Table 1). The INMS-measured mixing ratios for the inbound part of orbit 288 as reported by Serigano et al. (2022a) (data from Serigano et al., 2022b) are shown as yellow triangles (all species ∈ X) and purple triangles (only CH_4, N_2, and CO). LP-derived mixing ratio estimates for a population of heavy species potentially contributing to the secondary electron emission, denoted $f_{X'}$, as derived by Johansson et al. (2022) are shown as the dashed gray line with their errors.

variable. For example, this becomes relevant when discussing latitudinally confined influxes of ring material around the equator or along certain L-shells.

Altitudinal profiles of the estimated mixing ratio of heavy volatiles, f_{X,He^+} (Equation 10), for orbits 288 and 292 are shown in Figures 4 and 5 as gray dots, with a moving median over 20 points shown as blue lines. The shaded regions around the lines show the effect of setting k_{X,He^+} to the lowest or highest values among the rate coefficients for the He^+ reactions listed in Table 1. The derived mixing ratios around closest approach for both orbits are $\sim 2 \times 10^{-4}$, but otherwise the values for both orbits occasionally differ by more than an order of magnitude. The mixing ratios derived from Equation 10 show considerable variability with changing altitude/latitude for both orbit 288 and 292. Even more striking, in light of the fact that orbit 288 and 292 had quite similar geometries, is the fact that the f_{X,He^+} profiles obtained for the two orbits are so different. This could signal temporal variations in the influx or fate of the precipitating grains as argued for also in previous INMS-based studies (e.g., Miller et al., 2020; Waite et al., 2018). The region where the derived mixing ratios for the two orbits agree best is around closest approach, which could indicate a partial breakdown of the assumption of photochemical equilibrium at higher altitudes, or a more well-distributed ring influx at lower altitudes.

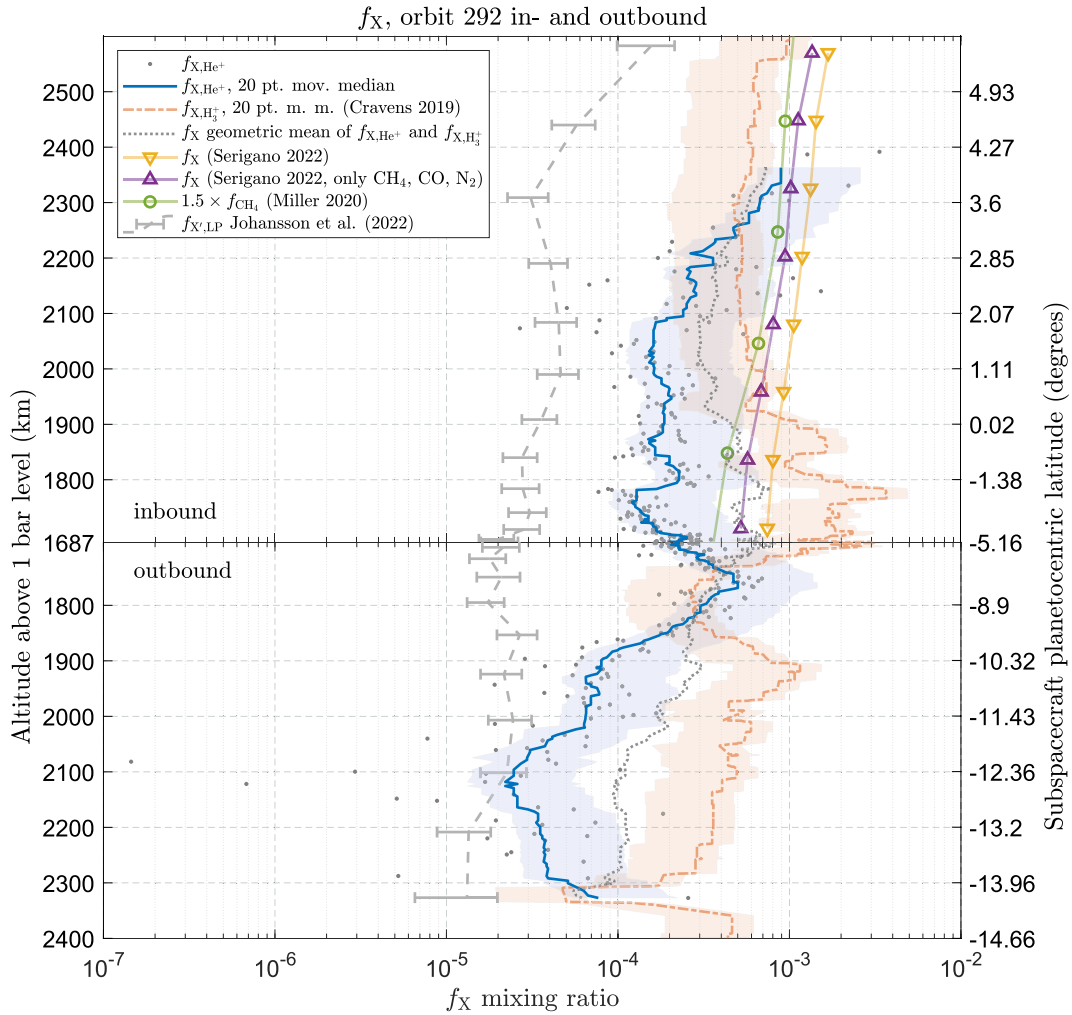

Figure 5. Mixing ratios f_X of species ∈X (in relation to H_2 density) for orbit 292 as gray dots, with a 20 point moving median as a blue line. The derived mixing ratio profile based on Equation 11 (Cravens, Moore, et al., 2019) is shown as a red dashed line (also 20 point moving mean), and a geometric mean of the two lines is shown as the dotted black line. The blue and red shaded areas around the lines mark the variation of f_X when setting k_X to the lowest or highest value, respectively (see Table 1). The INMS-measured mixing ratios for the inbound part of orbit 292 as reported by Serigano et al. (2022a) (data from Serigano et al., 2022b) are shown as yellow triangles (all species ∈X) and purple triangles (only CH_4, N_2, and CO). The mixing ratio of CH_4 as reported by Miller et al. (2020), multiplied by a factor 1.5, is shown as green circles. The multiplication factor is based on their averaged mixing ratio results, which indicate that CO and N_2 together are ∼50% as abundant as CH_4. LP-derived mixing ratio estimates for a population of heavy species potentially contributing to the secondary electron emission, denoted $f_{X'}$, as derived by Johansson et al. (2022) are shown as the dashed gray line with their errors.

There is some variety for the rate coefficient $k_3 = 4.1 \times 10^{-14}$ cm^3 s^{-1}, obtained from the UMIST database and based on Barlow (1984), among other studies. Moore et al. (2018) utilize $k_3 = 9.35 \times 10^{-15} + 2.04 \times 10^{-16}$ cm^3 s^{-1}, whereas (Anicich, 1993) list $k_3 = 8.3 \times 10^{-14} + 1.7 \times 10^{-14}$ cm^3 s^{-1}. Our chosen values thus fall between these, but the effect of choosing a lower or higher k_3 should be considered. Adopting the suggested values listed in Anicich (1993) decreases the discrepancy between modeled and measured [He^+] in Figure 3, but a discrepancy is still present. The effect of this change on the derived mixing ratio f_X is small (a reduction of 2%–20% for values above 10^{-4}), except for regions where the values are particularly small (approaching 10^{-5}), since in this case the first and second term in Equation 10 are of similar magnitude, which results in f_X values close to or less than zero. Conversely, using the much lower rate coefficients from Moore et al. (2018), the gap between modeled and measured [He^+] in Figure 3 widens significantly, and our derived f_X values increase accordingly.

The enhanced He^+ concentration seen over the altitude range 1,850–2,000 km during the inbound of orbit 288, mentioned in Section 2, at face value indicates a local or temporal decrease of f_{X,He^+}. This is reflected by the blue line in Figure 4. As a similar decrease is not seen during the inbound of orbit 292, temporal variability might be a possible explanation. However, we are cautious to not speculate much further on this, particularly so in light of how the results from our He^+-based method compare with results from Johansson et al. (2022). They conducted Langmuir probe sweep analysis with a special emphasis on the contribution to the current by secondary electron emission due to neutrals impacting the probe at high velocity. By assuming a common yield of 10% upon impact of any species potentially contributing to the secondary electron emission (due to a kinetic energy threshold, collisions from light species such as He and H_2 cannot contribute to the current), Johansson et al. (2022) were able to estimate the mixing ratio of this population, here denoted $f_{X'}$, along multiple Cassini trajectories. The profiles relevant for orbit 288 and 292 are shown as dashed gray lines in Figures 4 and 5. The authors argue that their mixing ratio estimate is mainly H_2O, but can also include CO_2, N_2, and CH_4. The contribution of each molecular species to their signal is not equal, and the authors tentatively argue that CO_2 and N_2 make up for a third of their signal, and that it is unaffected by CH_4. This comparison thus shares some similarities and ambiguities with our own, but the omission of CH_4 likely means that our estimate should exceed their values across the entire shown range. Our helium-based method and the method of Johansson et al. (2022) need not target precisely the same populations, but a comparison of results is nevertheless meaningful. For most of orbit 292 and for the outbound of orbit 288 the f_{X,He^+} values exceed their $f_{X'}$ values by roughly an order of magnitude. However, a drastically different relation is seen to prevail precisely during the aforementioned part of orbit 288 associated with a local maxima in the He^+ concentration (shaded area in Figure 3). It is difficult to reconcile why a pronounced reduction in the mixing ratio of heavy volatiles, needed to explain the local rise in the He^+ number density seen in Figure 3, would coincide with a comparatively high value of $f_{X'}$.

Regions with variations in f_{X,He^+} of an order of magnitude over along-trajectory-altitude (latitude) ranges of less than 100 km (a few degrees) are visible for both orbits. It is theorized that the surface temperature of grains varies as the grains precipitate through the atmosphere toward higher pressure regions (Hamil et al., 2018). Variability in the mixing ratio of heavy volatiles may partly be controlled by the conditions dictating whether substances are prone to evaporate from grains or to recondense on them. Highly volatile species may initially have been incorporated in the ring particles as hydrates, but from their phase diagrams (see, e.g., Figure 7 in Miller et al., 2020) it seems unlikely that CH_4, N_2, and CO, once released, would be subject to recondensation. Our He^+-based f_X values fall short in comparison to the mixing ratios of heavy volatiles inferred from direct INMS measurements (e.g., Miller et al., 2020; Serigano et al., 2022a; Waite et al., 2018). As covered in detail in Miller et al. (2020) and Moses et al. (2023) there is the possibility that a significant fraction of the neutrals detected by the INMS results from fast inflowing icy dust components vapourizing in the instrument. Moses et al. (2023) made different assumptions in their modeling work as to what the direct INMS measurements tell about the ambient gas and made comparisons of the respective model case output with remote sensing observations of the stratosphere (and with in situ measurements of the ionosphere). The model reproducibility of observations improved while working with the assumption that only the most volatile species—CH_4, N_2, and CO—were truly present in the gas phase anywhere near the level inferred from the direct measurements (their *Case B*). As seen in Figures 4 and 5, our He^+-based f_X values compare better with, but still fall short of, the inferred mixing ratio of these "super-volatiles" (purple and green triangles/circles). An improved agreement can in principle be achieved by assuming that a fraction of the measured CH_4, N_2, and CO also stem from impact vapourization, but we are cautious to not stretch this reasoning much further as the He^+-based method of estimating f_X may have its own limitations.

Major differences are seen in comparisons between the f_X profiles derived from helium ion chemistry (blue lines in Figures 4 and 5) and from hydrogen ion chemistry (red lines in Figures 4 and 5, shaded regions also created by setting k_{X,H_3^+} to minimum and maximum values). An explanation is still lacking for the peculiar altitudinal variations in the $H^+/H_3{}^+$ number density ratio observed both in orbit 288 and 292 (Cravens, Moore, et al., 2019; Moore et al., 2018). The associated mixing ratio conundrum in regards to M- and R-type species (which together make up the species $\in$X) has been considered (Moses et al., 2023; Vigren et al., 2022), but remains unresolved. Whatever eludes our understanding of the hydrogen ion chemistry in Saturn's ionosphere may or may not have an impact also on the helium ion chemistry. Upon closer inspection of the He^+-based and $H_3{}^+$-based f_X profiles, cases where a local maximum from one method lies near a local minimum from the other method can be seen. The reason for this can be speculated on, and the helium and hydrogen ion data show a similar, potentially anti-correlated, behavior. Signatures of gravity waves (Matcheva & Barrow, 2012) might be visible in the ion

data, but how this could result in a diverging profile for the two species and a more precise determination of the underlying cause(s) would require a dedicated follow-up study. Another possible explanation for the largest divergences between the helium- and hydrogen-derived mixing ratios could be a pronounced influx of water ice grains, which shift the lines in opposite directions due to the nature of the respective reaction rate coefficients (see Table 1). If, for example, water were to make up most of the infalling ring species in the region 2,000–1,800 km for orbit 288 inbound, the blue and red lines would move to higher and lower values closer to the edges of the shaded regions, respectively. This could facilitate a closer agreement between the two methods wherever water were to make up a larger fraction of the ring influx. The main issue with this reasoning is the high yield of water for secondary electron emission on the Langmuir probe, and at least for orbit 292 the results of Johansson et al. (2022) indicate a fairly low and stable fraction of water among the detected ring species throughout the analyzed region of this orbit. Their values for the inbound part of orbit 288 on the other hand might be compatible with the above hypothesis, as they show an increase in the LP-derived f_X where we see the largest discrepancy between the profiles derived from He^+ and H_3^+.

The dotted black lines in Figures 4 and 5 correspond to the geometric mean of the two f_X measures whenever both are available (taking a geometric mean instead of an arithmetic mean was loosely motivated by the fact that both f_X measures display strong variations even on a logarithmic scale). These show lesser variation and align better with the direct INMS measurements, particularly with those restricted to CH_4, N_2, and CO. The $f_{X'}$ values of Johansson et al. (2022) fall short of the averaged f_X values by a factor that typically lies in the range 5–10, with the exception of the inbound part of orbit 288. The level of agreement can be improved if in the analysis of Johansson et al. (2022) one were to reduce the assumed yield for secondary electron emission as neutrals impact the Langmuir probe from 10% to ∼1%–2%. The question should be raised whether such a reduction is reasonable in the light of the possibility, addressed by Moses et al. (2023), that the heavy volatiles in Saturn's ionosphere are dominated by CH_4, N_2, and CO, while Johansson et al. (2022) pictured H_2O impacts as the main driver of the secondary electron emission. We cannot provide a definite answer to this question, at least not at this stage. While experiments have been conducted for H_2O and N_2 impacts on relevant metal targets (Schmidt & Arends, 1985), indeed suggesting yields on the order of 10%, to the best of our knowledge no similar experiments involving impacts on metal targets of, for example, CH_4 and CO molecules have yet been conducted. The analysis by Johansson et al. (2022) thus also puts constraints on the abundance of N_2 among the volatile species.

4. Conclusions

The present study aimed to estimate the volume mixing ratios of heavy volatiles in Saturn's near equatorial ionosphere from in situ measurements of light ions and neutrals during Cassini's Grand Finale orbits. Based on the assumption of photochemical equilibrium at altitudes below ∼2,500 km we first showed that the dominant loss mechanism for He^+ ions in said region is through reactions with other species than H_2; namely heavier volatiles collectively denominated as ∈X. We proceeded by balancing the production- and loss rates of He^+ to arrive at an expression for the mixing ratio for these species, f_{X,He^+}, where the indexing reflects that He^+ chemistry was used to estimate the mixing ratio of species ∈X. The resulting mixing ratio profiles obtained for orbits 288 and 292 agree on values of $\sim 2 \times 10^{-4}$ near their respective closest approaches (∼1,700 km), but show considerable intraorbital (with altitude and latitude along the Cassini trajectory) as well as interorbital variations by an order of magnitude in either direction.

The f_{X,He^+} values differ notably from the f_{X,H_3^+} values from H_3^+ chemistry, obtained similarly as in Cravens, Moore, et al. (2019). To take some cover for potentially oversimplified modeling assumptions, we constructed mixing ratio profiles based on the geometric mean of the locally obtained values of f_{X,He^+} and f_{X,H_3^+}. These show lesser variation and agree somewhat better with the direct INMS measurements (Miller et al., 2020; Serigano et al., 2022a), especially when restricted to CH_4, N_2, and CO. A potential explanation for the latter could be similar to the basis for *Case B* as described by Moses et al. (2023): Only the most volatile species enter the atmosphere as vapor, and most of the INMS data are due to impact fragmentation of grain-bound species, which are thus also not available for reactions in the ionosphere.

While straightforward in their implementation and of potential use for future in situ based studies of gas- and ice giant's ionospheres, the He^+- and H_3^+-based approaches utilized in this work rely on the accuracy in the adapted reaction rate coefficients, observation-based input parameters and, not to be forgotten, in the underlying modeling

assumptions. The discrepancy between f_{X,He^+} and f_{X,H_3^+} profiles suggests, for one, that we are still struggling to adequately interpret the concentrations of the light ion species in Saturn's ionosphere.

Data Availability Statement

Cassini ephemeris data are available from NASA's Planetary Data System (PDS, https://pds-rings.seti.org/cassini). Cassini RPWS data likewise are available from the PDS (Wahlund, 2018). The derived INMS ion data used in the present study were provided by the INMS science team and are based on the INMS L1A data that are available from the PDS as well.

Acknowledgments
The research of J.D. and E.V. at the Swedish Institute of Space Physics is supported by the Swedish National Space Agency under Grant Dnr 143/18. J.H.W. was funded through Waite Science LLC from consulting funding from Southwest Research Institute. The authors thank the two anonymous reviewers for their helpful feedback.

References

Anicich, V. G. (1993). Evaluated bimolecular ion-molecule gas phase kinetics of positive ions for use in modeling planetary atmospheres, cometary comae, and interstellar clouds. *Journal of Physical and Chemical Reference Data*, *22*(6), 1469–1569. https://doi.org/10.1063/1.555940

Barlow, S. E. (1984). *The dynamics of stored ions and low temperature ion-molecule reactions (Unpublished doctoral dissertation)*. University of Colorado.

Browning, R., & Fryar, J. (1973). Dissociative photoionization of H_2 and D_2 through the $1s\sigma_g$ ionic state. *Journal of Physics B: Atomic and Molecular Physics*, *6*(2), 364–371. https://doi.org/10.1088/0022-3700/6/2/019

Chadney, J., Koskinen, T., Hu, X., Galand, M., Lavvas, P., Unruh, Y., et al. (2022). Energy deposition in Saturn's equatorial upper atmosphere. *Icarus*, *372*, 114724. https://doi.org/10.1016/j.icarus.2021.114724

Chamberlin, P. C., Woods, T. N., & Eparvier, F. G. (2008). Flare irradiance spectral model (FISM): Flare component algorithms and results. *Space Weather*, *6*(5), S05001. https://doi.org/10.1029/2007SW000372

Cravens, T. E., Moore, L., Waite, J. H., Perryman, R., Perry, M., Wahlund, J. E., et al. (2019). The ion composition of Saturn's equatorial ionosphere as observed by Cassini. *Geophysical Research Letters*, *46*(12), 6315–6321. https://doi.org/10.1029/2018GL077868

Cravens, T. E., Morooka, M., Renzaglia, A., Moore, L., Waite, J. H., Perryman, R., et al. (2019). Plasma transport in Saturn's low-latitude ionosphere: Cassini data. *Journal of Geophysical Research: Space Physics*, *124*(6), 4881–4888. https://doi.org/10.1029/2018JA026344

Cunto, W., Mendoza, C., Ochsenbein, F., & Zeippen, C. J. (1993). TOPbase at the CDS. *Astronomy and Astrophysics*, *275*, L5–L8.

Dreyer, J., Vigren, E., Johansson, F. L., Shebanits, O., Morooka, M., Wahlund, J.-E., et al. (2022). Identifying shadowing signatures of C ring ringlets and plateaus in Cassini data from Saturn's ionosphere. *The Planetary Science Journal*, *3*(7), 168. https://doi.org/10.3847/psj/ac7790

Dreyer, J., Vigren, E., Morooka, M., Wahlund, J.-E., Buchert, S. C., Johansson, F. L., & Waite, J. H. (2021). Constraining the positive ion composition in Saturn's lower ionosphere with the effective recombination coefficient. *The Planetary Science Journal*, *2*(1), 39. https://doi.org/10.3847/psj/abd6e9

Hamil, O., Cravens, T. E., Reedy, N. L., & Sakai, S. (2018). Fate of ice grains in Saturn's ionosphere. *Journal of Geophysical Research: Space Physics*, *123*(2), 1429–1440. https://doi.org/10.1002/2017JA024616

Huebner, W., & Mukherjee, J. (2015). Photoionization and photodissociation rates in solar and blackbody radiation fields. *Planetary and Space Science*, *106*, 11–45. https://doi.org/10.1016/j.pss.2014.11.022

Johansson, F. L., Vigren, E., Waite, J. H., Miller, K., Eriksson, A. I., Edberg, N. J. T., & Dreyer, J. (2022). Implications from secondary emission from neutral impact on Cassini plasma and dust measurements. *Monthly Notices of the Royal Astronomical Society*, *515*(2), 2340–2350. https://doi.org/10.1093/mnras/stac1856

Matcheva, K. I., & Barrow, D. J. (2012). Small-scale variability in Saturn's lower ionosphere. *Icarus*, *221*(2), 525–543. https://doi.org/10.1016/j.icarus.2012.08.022

McElroy, D., Walsh, C., Markwick, A. J., Cordiner, M. A., Smith, K., & Millar, T. J. (2013). The UMIST database for astrochemistry 2012. *Astronomy and Astrophysics*, *550*, A36. https://doi.org/10.1051/0004-6361/201220465

Miller, K., Waite, J., Perryman, R., Perry, M., Bouquet, A., Magee, B., et al. (2020). Cassini INMS constraints on the composition and latitudinal fractionation of Saturn ring rain material. *Icarus*, *339*, 113595. https://doi.org/10.1016/j.icarus.2019.113595

Moore, L., Cravens, T. E., Müller-Wodarg, I., Perry, M. E., Waite, J. H., Perryman, R., et al. (2018). Models of Saturn's equatorial ionosphere based on in situ data from Cassini's grand finale. *Geophysical Research Letters*, *45*(18), 9398–9407. https://doi.org/10.1029/2018gl078162

Morooka, M. W., Wahlund, J., Hadid, L. Z., Eriksson, A. I., Edberg, N. J. T., Vigren, E., et al. (2019). Saturn's dusty ionosphere. *Journal of Geophysical Research: Space Physics*, *124*(3), 1679–1697. https://doi.org/10.1029/2018ja026154

Moses, J. I., Brown, Z. L., Koskinen, T. T., Fletcher, L. N., Serigano, J., Guerlet, S., et al. (2023). Saturn's atmospheric response to the large influx of ring material inferred from Cassini INMS measurements. *Icarus*, *391*, 115328. https://doi.org/10.1016/j.icarus.2022.115328

Perry, M. E., Waite, J. H., Mitchell, D. G., Miller, K. E., Cravens, T. E., Perryman, R. S., et al. (2018). Material flux from the rings of Saturn into its atmosphere. *Geophysical Research Letters*, *45*(19), 10093–10100. https://doi.org/10.1029/2018GL078575

Schmidt, R., & Arends, H. (1985). Laboratory measurement on impact ionization by neutrals and floating potential of a spacecraft during encounter with Halley's Comet. *Planetary and Space Science*, *33*(6), 667–673. https://doi.org/10.1016/0032-0633(85)90048-0

Serigano, J., Hörst, S. M., He, C., Gautier, T., Yelle, R., Koskinen, T., et al. (2022b). *Data associated with the publication: Compositional measurements of Saturn's upper atmosphere and rings from Cassini INMS: An extended analysis of measurements from Cassini's grand finale orbits*. Johns Hopkins University Data Archive. https://doi.org/10.7281/T1/LJ9FLW

Serigano, J., Hörst, S. M., He, C., Gautier, T., Yelle, R. V., Koskinen, T. T., et al. (2022a). Compositional measurements of Saturn's upper atmosphere and rings from Cassini INMS: An extended analysis of measurements from Cassini's grand finale orbits. *Journal of Geophysical Research: Planets*, *127*(6), e2022JE007238. https://doi.org/10.1029/2022JE007238

Sundström, G., Mowat, J. R., Danared, H., Datz, S., Broström, L., Filevich, A., et al. (1994). Destruction rate of H_3^+ by low-energy electrons measured in a storage-ring experiment. *Science*, *263*(5148), 785–787. https://doi.org/10.1126/science.263.5148.785

Theard, L. P., & Huntress, W. T. (1974). Ion-molecule reactions and vibrational deactivation of H_2^+ ions in mixtures of hydrogen and helium. *Journal of Chemical Physics*, *60*(7), 2840–2848. https://doi.org/10.1063/1.1681453

Vigren, E., Dreyer, J., Eriksson, A. I., Johansson, F. L., Morooka, M., & Wahlund, J.-E. (2022). Empirical photochemical modeling of Saturn's ionization balance including grain charging. *The Planetary Science Journal*, *3*(2), 49. https://doi.org/10.3847/psj/ac4eee

Wahlund, J.-E. (2018). Cassini SS/S RPWS derived Langmuir probe sweep V1.0 [Dataset]. NASA Planetary Data System. https://doi.org/10.17189/1519612

Waite, J. H., Perryman, R. S., Perry, M. E., Miller, K. E., Bell, J., Cravens, T. E., et al. (2018). Chemical interactions between Saturn's atmosphere and its rings. *Science*, *362*, 6410. https://doi.org/10.1126/science.aat2382

Yelle, R. V., Serigano, J., Koskinen, T. T., Hörst, S. M., Perry, M. E., Perryman, R. S., & Waite, J. H. (2018). Thermal structure and composition of Saturn's upper atmosphere from Cassini/ion neutral mass spectrometer measurements. *Geophysical Research Letters*, *45*(20), 10951–10958. https://doi.org/10.1029/2018GL078454